

Observation of many-body quantum phase transitions beyond the Kibble-Zurek mechanism

Qi Huang,¹ Ruixiao Yao,² Libo Liang,¹ Shuai Wang,² Qinpei Zheng,¹ Dingping Li,³
Wei Xiong,¹ Xiaoji Zhou,¹ Wenlan Chen,^{2,4,*} Xuzong Chen,^{1,†} and Jiazhong Hu^{2,4,‡}

¹*School of Electronics Engineering and Computer Science, Peking University, Beijing 100871, China*

²*Department of Physics and State Key Laboratory of Low Dimensional
Quantum Physics, Tsinghua University, Beijing, 100084, China*

³*School of Physics, Peking University, Beijing 100871, China*

⁴*Frontier Science Center for Quantum Information, Beijing, 100084, China*

The quantum critical behaviors of many-body phase transition is one of the most fascinating yet challenging questions in quantum physics. Here, we improved the band-mapping method to investigate the quantum phase transition from superfluid to Mott insulators, and we observed the critical behaviors of quantum phase transitions in both dynamical steady-state-relaxation region and phase-oscillation region. Based on various observables, two different values for the same quantum critical parameter are observed. This result is beyond a universal-scaling-law description of quantum phase transitions known as the Kibble-Zurek mechanism, and suggests that multiple quantum critical mechanisms are competing in many-body quantum phase transition experiments.

The non-equilibrium quantum physics is one of the most challenging topics in quantum physics, related with many different areas such as quantum matters [1, 2], many-body correlations [3, 4], and quantum simulation [5–9]. One central question among the non-equilibrium quantum physics is how to understand the quantum critical behaviors and the dynamics of the quantum phase transitions (QPT). The Kibble-Zurek mechanism (KZM) [10, 11] originating from thermodynamics [12–14], describes the dynamics of QPT with symmetry breaking [15–19], where the order parameter can be well-defined and the quantum critical behaviors have a universal scaling-law dependence on the external ramping speed. As for the development of QPT, the energy gap instead of the symmetry breaking becomes the critical condition in phase transitions. Thus, it becomes interesting to investigate many-body quantum phase transitions entering symmetry-conserved phases with open energy gaps, which is on the opposite side of the conventional KZM.

The superfluid (SF) to Mott insulators (MI) phase transition is one of the most important QPT in many-body physics. Seminal experiments [20, 21] explored the KZM based on transitions from symmetry-conserved MI to symmetry-broken SF with gap closing where the measured quantum critical parameter cannot reach the consistency with the theoretical predictions [22, 23]. Here, we investigate the many-body QPT, where the system transits from the SF phase (gapless symmetry-broken) to the MI phase (gapped symmetry-conserved) with an improved band-mapping method. In such gap-opening QPT, the quantum criticality is described by the energy gap Δ versus the distance g to quantum critical point in

phase diagrams with a scaling law $\Delta \propto |g|^{\nu z}$ where νz is a quantum critical parameter. The value of νz decides the spatial-temporal universal dynamics in KZM [16, 24–29]. Based on various observables, we extract out two different values for the same critical parameter νz . Both values were predicted theoretically [22, 23] and are consistent with our data, but they are not allowed to appear in the same phase transition according to the KZM due to the universality. Besides, we observe dynamical steady-phase relaxations within the KZM frame transiting into non-steady-phase oscillations which is beyond the KZM frame. In fact, the gap opening allows different values of critical parameters to exist in the same QPT, protects phase-oscillations, and thus boosts the many-body QPT beyond the conventional symmetry-breaking KZM.

Our experiment is performed in a three-dimensional optical lattice formed by three standing waves perpendicular to each other at wavelength $\lambda = 1064$ nm (Fig. 1a), and the magnetic field is applied along the z axis. We create Bose-Einstein condensations of ⁸⁷Rb atoms in $|F = 1, m_F = -1\rangle$ and then load them into 3D homogeneous lattices with trap depth $V = 5E_r$ and atom number of $N = 1.1 \times 10^5$. Here V is the trap depth generated by one lattice beam and $E_r = h \times 2$ kHz is the recoil energy of the lattice beams. Due to the Gaussian shape of the lattice beams, the lattices are printed by an external harmonic trap with homogeneous radial vibrational frequencies $\sim 2\pi \times 20$ Hz. The system is described by a Bose-Hubbard model in an external harmonic trap [22, 30]:

$$H = -J \sum_{\langle i,j \rangle} (\hat{a}_i^\dagger \hat{a}_j + h.c.) + \frac{1}{2} U \sum_i \hat{n}_i (\hat{n}_i - 1) + \sum_i \left(\frac{1}{2} m \omega_0^2 r_i^2 - \mu \right) \hat{n}_i, \quad (1)$$

where a_i (or a_i^\dagger) is the annihilation (or creation) operator

* cwllaser@ultracold.cn

† xuzongchen@pku.edu.cn

‡ hujiazhong01@ultracold.cn

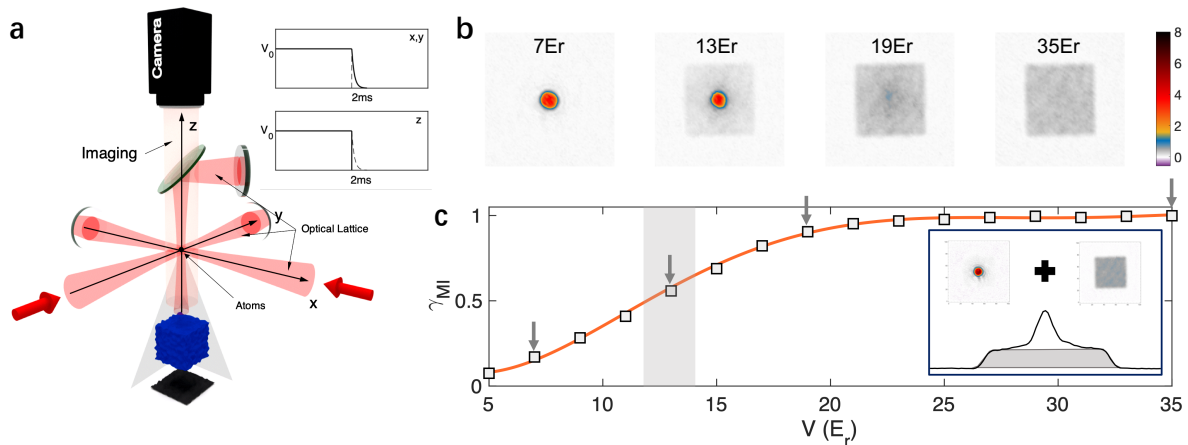


FIG. 1. **Experimental setup and improved band-mapping method.** **a**, Three standing waves at 1064 nm form 3D optical lattices for ^{87}Rb , and the absorption images are applied along the z direction. The inset: The z lattice is turned off instantaneously while the x and y lattices are ramped down in 2 ms for the band mapping. **b**, The band mapping profiles performed at homogeneous 3D trap depth V of 7, 13, 19, and $35E_r$, where E_r is the recoil energy of the lattice beam. **c**, The MI fraction γ_{MI} versus the trap depth V for the SF-MI phase transitions. The shadow area locates quantum phase transition at $V_c = 13E_r$ for $\bar{n} = 1$'s lobe. Grey arrows indicate data in the panel b. The inset shows the decomposition of quasi-momentum profiles and analysis of γ_{MI} . Error bars (one standard deviation) are smaller than the marker size.

of a boson at the lattice site i , J is the tunneling coefficient depending on the lattice trap depth, U is the on-site interaction, μ is the chemical potential, and $\frac{1}{2}m\omega_0^2 r_i^2$ describes the potential of the external harmonic trap.

Comparing to the previous band-mapping method [31] requiring adiabatically turning off three lattice beams, here we instantaneously turn off the z lattice that is along the imaging direction (Fig. 1a). The atomic gas expands along z quickly, releases the interaction energy, and the momentum distribution along z does not contribute to the final band-mapping. It helps to avoid the fast relaxations in the $x-y$ plane in the subsequent expansion. At the same time of turning off the z lattice, we start to ramp down the x and y lattices in 2 ms, which is slow enough to adiabatically convert the quasi-momentum into the real momentum. Then the time-of-flight is applied to measure the momentum distribution in the $x-y$ plane. By using this technique, we are able to obtain a better resolution of MI quasi-momentum distributions (Fig. 1b and see Supplemental Informations (SI) for comparisons), where the quasi-momentum distribution in the first Brillouin zone is exactly mapped to a square shape and displays a flat plateau, while the SF component corresponds to a narrow and sharp peak at the zero-momentum point. This helps us to distinguish the phase components of SF and MI (Fig. 1b). We define the MI fraction γ_{MI} based on the band mapping, where it is defined as the ratio of the integrated optical depth of the flat plateau divided by the total integrated optical depth (Fig. 1c and SI).

To study dynamics of QPT, each time we prepare the superfluid at $V_0 = 5E_r$ and then hold it for 20 ms. After the holding, we ramp up the trap depth V linearly with a ramping rate k (Fig. 2a). For each k , we per-

form the band mapping at different V and measure the corresponding MI fraction γ_{MI} (Fig. 2b). According to Ref. [30], the MI start to appear at $V_c = 13E_r$ for ^{87}Rb . We find two different response regions before and after ramping through V_c . In the SF region, the system responds to the ramping rapidly due to its gapless nature. We calculate the response time τ_{SF} by defining the time to reach $\gamma_{MI} = 0.6$ and obtain a scaling-law dependence $\tau_{SF} \propto k^{-0.91(3)}$, slightly delayed from the ideal instant response k^{-1} . The experimental extraction also agrees well with our numerical simulation by the Gutzwiller mean field theory (GMFT) (Fig. 2c). However, once the trap depth is above V_c , γ_{MI} starts to furcate and show retarded or oscillating responses depending on k .

For a slow ramp ($k \leq 4E_r/\text{ms}$), the response in the MI region is trying to approach a steady state with a dynamical relaxation time τ_{MI} . In Fig 2d, we extract τ_{MI} based on the time duration to reach $\gamma_{MI} = 0.9$ from the time at trap depth $13E_r$ [16]. It shows a scaling-law dependency: $\tau_{MI} \propto k^{-0.53(5)}$. In SI, we verify that the exponent near -0.5 is not sensitive to the end point MI fraction γ_{MI} we choose. The KZM predicts the dependence of the critical time τ on the ramping rate k in a form of [16, 24–26]

$$\tau \propto k^{-\frac{\nu z}{1+\nu z}}. \quad (2)$$

Based on this form, we obtain the critical parameter $\nu z = 1.1(2)$ by measuring the MI dynamical relaxation time and infer $\nu = 1/2$ & $z = 2$ corresponding to the off-tip critical parameters with linear gap opening in the SF-MI phase diagram [22]. To show the quantum criticality, we rescale the horizontal axis of Fig. 2b at V_c , the different sets of $\gamma_{MI} - k$ data fall into one universal curve (Fig. 2e)

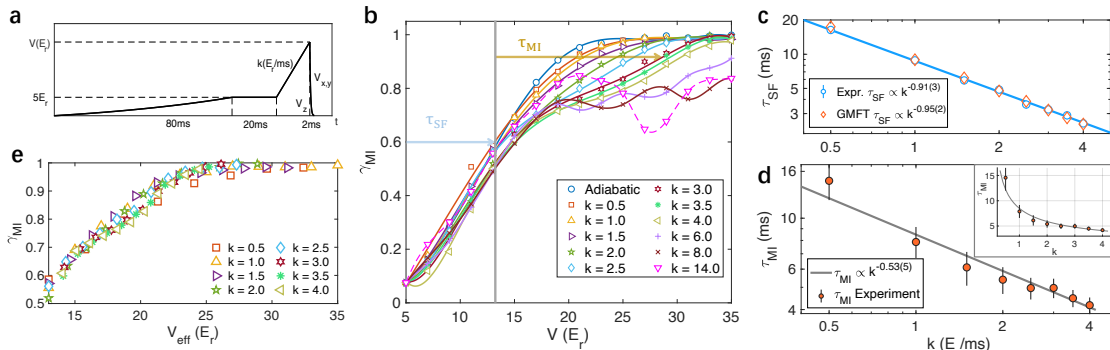


FIG. 2. **Dynamical response of SF-MI phase transitions.** **a**, The time sequence of the trap depth V ramping. The first stage of 80 ms and the second stage of 20 ms are for preparing superfluid samples from the condensates. The third stage is the linear ramp with a ramping rate k and the atoms experience phase transitions during this stage. The final stage is the band mapping to distinguish the components of SF and MI. **b**, The MI fraction γ_{MI} versus trap depth V for different k . The scattered markers are the experimental data and the solid lines are the polynomial fits (see SI). A furcation appears at critical point $V_c = 13E_r$. And γ_{MI} approaches 1 for different ramping rate k while k is small. When k gets larger, γ_{MI} starts to oscillate with retarding in thermalization. The pink triangles denote the dynamics of the case at $k = 14E_r/\text{ms}$ which oscillates drastically and fail to relax. Here we label how we define the SF response time τ_{SF} (time to reach $\gamma_{MI} = 0.6$) and the MI dynamical relaxation time τ_{MI} (time between $\gamma_{MI} = 0.6$ and $\gamma_{MI} = 0.9$) on the plot. **c**, τ_{SF} versus k . The blue circles are the experimental data and the blue solid line is the fit based on power laws with $\tau_{SF} \sim k^{-0.91(3)}$. The red diamonds are the GMFT results with a fit $\tau_{SF} \propto k^{-0.95(2)}$. **d**, τ_{MI} versus k . The red filled circles are the extracted data and the black solid line is the fit with $\tau_{MI} \sim k^{-0.53(5)}$ where we obtain $\nu z = 1.1(2)$. **e**, The universal response of γ_{MI} versus the rescaled trap depth V_{eff} . The horizontal axis is rescaled according to $V_{eff} = (V - V_c)k^{-(1-0.53)} + V_c$ where k is in the unit of E_r/ms . Error bars correspond to one standard deviation.

in the MI region. This shows the universality of the KZM if we only consider τ_{MI} under a slow ramp k .

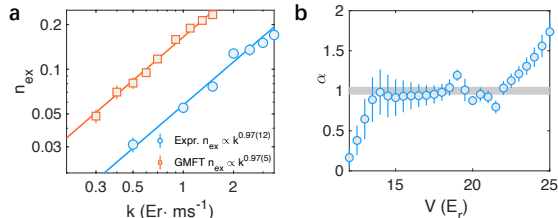


FIG. 3. **Excitation fraction n_{ex} in the MI region.** **a**, $n_{ex}(k)$ calculated around $V \sim 18E_r$ (SI). Blue circles are the experimental results and the orange squares are from GMFT simulations. The dashed line is the fit of data with $n_{ex} \sim k^\alpha$ where $\alpha = 0.97(12)$, and the simulations provide $\alpha = 0.97(5)$. We obtain $\nu z = 0.48(9)$ based on n_{ex} versus k . **b**, The fitted scaling coefficient α is robust against the chosen trap depth V , as long as $V > 13E_r$ (goes through phase transition) and $V < 19E_r$ (far from deep MI region). Error bars correspond to one standard deviation.

Besides a scaled relaxation time, the KZM also gives universally scaled defects distributions while crossing the phase transition. Here we use the excitation fraction n_{ex} to characterize the defects, where it describes how many atoms are excited comparing to ground-state Mott insulators. n_{ex} follows the form of [24, 27–29]:

$$n_{ex} \propto k^{\frac{d\nu}{1+\nu z}}. \quad (3)$$

Here $d = 3$ corresponds to the case of 3D optical lat-

tices. We analyze the excitation fraction as the components of MI fractions deviated from its adiabatic value [20]: $n_{ex}(V, k) = \gamma_{MI}(V, \text{adia}) - \gamma_{MI}(V, k)$. For $V > V_c$, $n_{ex}(V, k)$ characterizes how many atoms are not in the ground state and retain the additional phase coherence due to the non-equilibrium dynamics. In Fig. 3a, we plot $n_{ex}(V, k)$ and obtain a scaling-law $n_{ex} \propto k^{0.97(12)}$. (Fig. 3a). The definition of $n_{ex}(V, k)$ depends on how we choose each particular V , but the fitted-exponent's value is robust against the changing of V (Fig. 3b). Based on Eq. 3, we get $\nu z = 0.48(9)$ where we infer $\nu = 1/2$ & $z = 1$ corresponding to the on-tip critical parameters with square-root gap opening in the SF-MI phase diagram [22]. To further understand this and support our observations, we apply GMFT and find the remained superfluid due to the non-equilibrium dynamics has a scaling factor of 0.97(5), consistent with our experimental observation.

For a fast ramp ($k \geq 6E_r/\text{ms}$), the system response gradually enters a non-steady-state region where γ_{MI} oscillates with time. This provides a smooth connection from the adiabatically ramping to the instantaneous turning on [32]. When the ramping is fast, the multiple-atom occupancies in the SF are frozen immediately without relaxations. However, the phase coherence between single- and multiple- occupancies does not disappear immediately and oscillates at the frequency of U/\hbar . To visualize the oscillation, we hold the lattice for a time interval t after the ramping, where a larger k leads to a

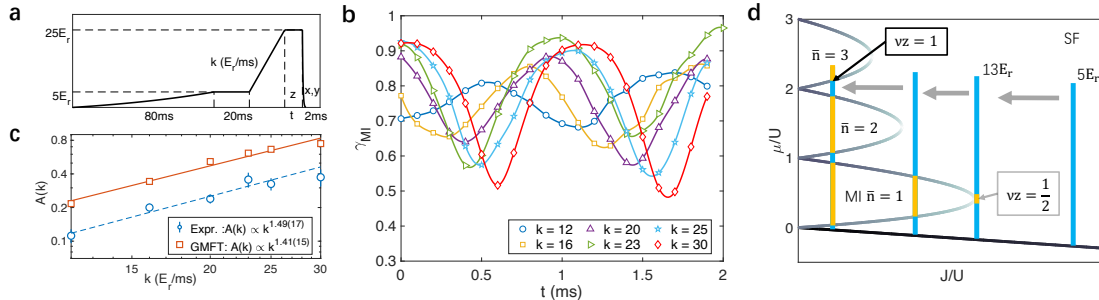


FIG. 4. **Phase-oscillations under a fast ramp.** **a**, Time sequences for oscillation measurements. The atoms are held at $V = 25E_r$ for a varying time t . **b**, γ_{MI} oscillates versus time t for different k . The solid lines are from cubic splines. **c**, The oscillation amplitude A versus k . Blue circles are the data and the red squares are the GMFT simulations. Two dashed lines are the fits based on power laws. For experimental data we obtain $A(k) \propto k^{1.49(17)}$, and the GMFT give us $A(k) \propto k^{1.41(15)}$. **d**, A schematic plot for the dynamics in the SF-MI phase diagram. The blue lines represents our actual system and the on- or off-tip locations are labeled by arrows with $\nu z = 1/2$ or 1. The on-tip location has square-root gap opening and the off-tip one has linear gap opening.

larger oscillation amplitude A (Fig. 4a and b). We apply the fit and obtain $A \propto k^{1.49(17)}$ (Fig. 4c). GMFT calculations are also performed to support this result, where $A \propto k^{1.41(15)}$ is obtained. The oscillation amplitude A characterizes the excitation fraction for such non-steady phase transitions. Since this lack of thermalization and subsequent oscillation is the direct consequence of the gap-opening process, the scaling dependence $A \sim k^{3/2}$ provides a new relation for the critical behaviors in the non-steady-state region which was not explored by conventional KZM.

Based on different observables, we get two different values for the same quantum critical parameter νz , namely $\nu z = 1$ for the MI dynamical relaxation time τ_{MI} and $\nu z = 1/2$ for the excitation fraction n_{ex} . According to conventional KZM, the universality of the quantum criticality predicts the same value of νz for different observables in the same QPT. Thus, our measurement results intradict the conventional KZM. According to previous studies [22, 23], νz is either 1 or 1/2 depending on whether the phase transition point is off- or on-tip and how the gaps open in the SF-MI phase diagram (Fig. 4d). Due to the harmonic trap and fixed atom number in our experiment, we probe the phase transition with an unfixed chemical potential, corresponding to a line, not a point in the phase diagram. The center filling of the final stage of MI is approximately $\bar{n} \sim 3$. In the scenario of a slow ramp, the MI first appear in the center of the harmonic trap while the trap depth is not deep enough. Because the local gap opens as $\Delta \propto |g|^{1/2}$, the early-formed MI defects appear in the trap center under the quantum criticality of $\nu z = 1/2$. Later when the trap depth increases, the total system enters the region of off-tip phase transitions where the gap $\Delta \propto |g|$ opens linearly with $\nu z = 1$. However, the previously-generated defects are still protected by the energy gaps under $U(1)$ symme-

tries with $\nu z = 1/2$. This is how both νz appear in the same QPT experiment. If the QPT is performed in the opposite direction from gapped phases to gapless phases as in the previous experiments [20, 21], the gapless excitations due to broken symmetries will smear out early-formed defects with later dynamics and it will makes the different values of quantum critical parameter becoming indistinguishable. For a fast ramp, the system is immediately frozen into deep Mott insulators with failed relaxations due to large energy gaps, where the actual dynamics versus the excitation fractions or the correlation length is still an unexplored regime for non-equilibrium physics and waits for further investigations.

In conclusion, we observe the many-body quantum phase transition from gapless symmetry-broken phases to gapped symmetry-conserved phases. The critical behaviors change from retarded relaxations to phase oscillations which is beyond the KZM frame. Even within the steady-state-relaxation regime, two different values for one critical parameter νz are observed which is not allowed by the conventional KZM. The gap opening provides and protects different critical-mechanism competitions in the dynamics of many-body phase transitions. We believe this inspires further investigations in the phase transition of symmetry-conserved gapped systems and the non-equilibrium physics.

We thank Hui Zhai, Joerg Schmiedmayer, Jakub Zakrzewski and Bogdan Damski for helpful discussions. The numerical simulations are performed on High-Performance-Computing Platform of Peking University. This work is supported by the National Natural Science Foundation of China (Grants No. 91736208, 11920101004, 61727819, 11934002, 11974202, 61975092) and the National Key Research and Development Program of China (Grant No. 2016YFA0301501).

- [1] Frank Wilczek, “Quantum time crystals,” *Phys. Rev. Lett.* **109**, 160401 (2012).
- [2] N. Goldman and J. Dalibard, “Periodically driven quantum systems: Effective hamiltonians and engineered gauge fields,” *Phys. Rev. X* **4**, 031027 (2014).
- [3] Dmitry A. Abanin, Ehud Altman, Immanuel Bloch, and Maksym Serbyn, “Colloquium: Many-body localization, thermalization, and entanglement,” *Rev. Mod. Phys.* **91**, 021001 (2019).
- [4] Rahul Nandkishore and David A. Huse, “Many-body localization and thermalization in quantum statistical mechanics,” *Annual Review of Condensed Matter Physics* **6**, 15–38 (2015).
- [5] P. C. Hendry, N. S. Lawson, R. A. M. Lee, P. V. E. McClintock, and C. D. H. Williams, “Generation of defects in superfluid ^4He as an analogue of the formation of cosmic strings,” *Nature* **368**, 315–317 (1994).
- [6] C. Bäuerle, Yu. M. Bunkov, S. N. Fisher, H. Godfrin, and G. R. Pickett, “Laboratory simulation of cosmic string formation in the early universe using superfluid ^3He ,” *Nature* **382**, 332–334 (1996).
- [7] Nir Navon, Alexander L. Gaunt, Robert P. Smith, and Zoran Hadzibabic, “Emergence of a turbulent cascade in a quantum gas,” *Nature* **539**, 72–75 (2016).
- [8] Sebastian Erne, Robert Bücke, Thomas Gasenzer, Jürgen Berges, and Jörg Schmiedmayer, “Universal dynamics in an isolated one-dimensional bose gas far from equilibrium,” *Nature* **563**, 225–229 (2018).
- [9] Maximilian Prüfer, Philipp Kunkel, Helmut Strobel, Stefan Lannig, Daniel Linnemann, Christian-Marcel Schmied, Jürgen Berges, Thomas Gasenzer, and Markus K. Oberthaler, “Observation of universal dynamics in a spinor bose gas far from equilibrium,” *Nature* **563**, 217–220 (2018).
- [10] T W B Kibble, “Topology of cosmic domains and strings,” *Journal of Physics A: Mathematical and General* **9**, 1387–1398 (1976).
- [11] W. H. Zurek, “Cosmological experiments in superfluid helium?” *Nature* **317**, 505–508 (1985).
- [12] Bumsuk Ko, Jee Woo Park, and Y. Shin, “Kibble–zurek universality in a strongly interacting fermi superfluid,” *Nature Physics* **15**, 1227–1231 (2019).
- [13] Nir Navon, Alexander L. Gaunt, Robert P. Smith, and Zoran Hadzibabic, “Critical dynamics of spontaneous symmetry breaking in a homogeneous bose gas,” *Science* **347**, 167–170 (2015).
- [14] Chad N. Weiler, Tyler W. Neely, David R. Scherer, Ashton S. Bradley, Matthew J. Davis, and Brian P. Anderson, “Spontaneous vortices in the formation of bose–einstein condensates,” *Nature* **455**, 948–951 (2008).
- [15] Pietro Silvi, Giovanna Morigi, Tommaso Calarco, and Simone Montangero, “Crossover from classical to quantum kibble-zurek scaling,” *Phys. Rev. Lett.* **116**, 225701 (2016).
- [16] L. W. Clark, L. Feng, and C. Chin, “Universal space-time scaling symmetry in the dynamics of bosons across a quantum phase transition,” *Science* **354**, 606–610 (2016).
- [17] Alexander Keesling, Ahmed Omran, Harry Levine, Hannes Bernien, Hannes Pichler, Soonwon Choi, Rhine Samajdar, Sylvain Schwartz, Pietro Silvi, Subir Sachdev, Peter Zoller, Manuel Endres, Markus Greiner, Vladan Vuletić, and Mikhail D. Lukin, “Quantum kibble–zurek mechanism and critical dynamics on a programmable rydberg simulator,” *Nature* **568**, 207–211 (2019).
- [18] M. Anquez, B. A. Robbins, H. M. Bharath, M. Boguslawski, T. M. Hoang, and M. S. Chapman, “Quantum kibble-zurek mechanism in a spin-1 bose-einstein condensate,” *Phys. Rev. Lett.* **116**, 155301 (2016).
- [19] L.-Y. Qiu, H.-Y. Liang, Y.-B. Yang, H.-X. Yang, T. Tian, Y. Xu, and L.-M. Duan, “Observation of generalized kibble-zurek mechanism across a first-order quantum phase transition in a spinor condensate,” *Science Advances* **6** (2020), 10.1126/sciadv.aba7292.
- [20] David Chen, Matthew White, Cecilia Borries, and Brian DeMarco, “Quantum quench of an atomic mott insulator,” *Phys. Rev. Lett.* **106**, 235304 (2011).
- [21] Simon Braun, Mathis Friesdorf, Sean S. Hodgman, Michael Schreiber, Jens Philipp Ronzheimer, Arnau Riera, Marco del Rey, Immanuel Bloch, Jens Eisert, and Ulrich Schneider, “Emergence of coherence and the dynamics of quantum phase transitions,” *Proceedings of the National Academy of Sciences* **112**, 3641–3646 (2015).
- [22] Matthew P. A. Fisher, Peter B. Weichman, G. Grinstein, and Daniel S. Fisher, “Boson localization and the superfluid-insulator transition,” *Phys. Rev. B* **40**, 546–570 (1989).
- [23] Subir Sachdev, *Quantum Phase Transitions*, 2nd ed. (Cambridge University Press, 2011).
- [24] D. Pekker, B. Wunsch, T. Kitagawa, E. Manousakis, A. S. Sørensen, and E. Demler, “Signatures of the superfluid to mott insulator transition in equilibrium and in dynamical ramps,” *Phys. Rev. B* **86**, 144527 (2012).
- [25] Keita Shimizu, Takahiro Hirano, Jonghoon Park, Yoshihito Kuno, and Ikuo Ichinose, “Dynamics of first-order quantum phase transitions in extended bose–hubbard model: from density wave to superfluid and vice versa,” *New Journal of Physics* **20**, 083006 (2018).
- [26] Keita Shimizu, Yoshihito Kuno, Takahiro Hirano, and Ikuo Ichinose, “Dynamics of a quantum phase transition in the bose-hubbard model: Kibble–zurek mechanism and beyond,” *Phys. Rev. A* **97**, 033626 (2018).
- [27] Anatoli Polkovnikov, “Universal adiabatic dynamics in the vicinity of a quantum critical point,” *Phys. Rev. B* **72**, 161201 (2005).
- [28] A. Bermudez, D. Patanè, L. Amico, and M. A. Martin-Delgado, “Topology-induced anomalous defect production by crossing a quantum critical point,” *Phys. Rev. Lett.* **102**, 135702 (2009).
- [29] A Bermudez, L Amico, and M A Martin-Delgado, “Dynamical delocalization of majorana edge states by sweeping across a quantum critical point,” *New Journal of Physics* **12**, 055014 (2010).
- [30] Markus Greiner, Olaf Mandel, Tilman Esslinger, Theodor W. Hänsch, and Immanuel Bloch, “Quantum phase transition from a superfluid to a mott insulator in a gas of ultracold atoms,” *Nature* **415**, 39–44 (2002).
- [31] Michael Köhl, Henning Moritz, Thilo Stöferle, Kenneth Günter, and Tilman Esslinger, “Fermionic atoms in a three dimensional optical lattice: Observing fermi surfaces, dynamics, and interactions,” *Phys. Rev. Lett.* **94**, 080403 (2005).
- [32] Markus Greiner, Olaf Mandel, Theodor W. Hänsch, and Immanuel Bloch, “Collapse and revival of the matter wave field of a bose–einstein condensate,” *Nature* **419**, 51–54 (2002).

Supplemental Informations for Observation of many-body quantum phase transitions beyond the Kibble-Zurek mechanism

Improved band mapping

The conventional band-mapping method requires adiabatically ramping down of all lattice beams for a 3D optical lattice. The purpose of adiabatic ramping is to convert the lattice quasi momentum into the free-space real momentum. In the Mott insulators phase, each atom is tightly trapped within one site which corresponds to the superposition of all the Bloch function with possible momenta within one band (Wannier function). Therefore, it is expected to be a uniform distribution over the first Brillouin zone.

However, due to the strong interaction in the Mott insulators region, the on-site interaction energy U alters the final momentum distributions during the time-of-flight imaging. In our improved version of band-mapping, we turn off the z lattice instantaneously and ramp down the x and y directions. The interaction energy is released into the imaging direction without affecting the other two directions, and this will give a better conversion from the quasi-momentum in the first Brillouin zone into the real momentum in the free space. Here we plot Fig. 5 to directly compare two methods at the different trap depth. Our method gives an exact square shape with a flat plateau for deep Mott insulators. It also gives a better resolution to distinguish two phases (SF and MI) in the intermediate region.

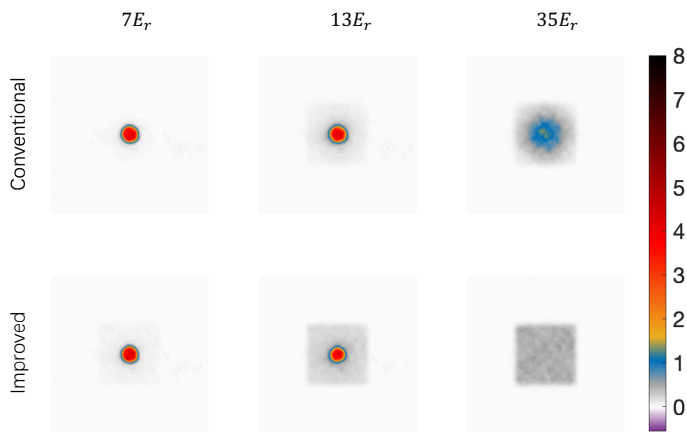


FIG. 5. **Improvement of band mapping.** The conventional and improved BM are plotted at $V = 7E_r$, $13E_r$ (Critical Phase), $35E_r$ (Deep MI). In the SF region, two methods give similar results. While interaction increases, our method starts to show a much flatter plateau. When the system reaches the deep Mott insulators, our method gives the exact momentum distribution in the first Brillouin zone. For comparison, the conventional method gives a central peak in the middle sometimes cannot be fully distinguished from the superfluid peak.

Analysis of Mott insulators fraction

The Mott insulators fraction γ_{MI} is defined as the fraction of the flat plateau in the quasi-momentum distribution. In the practical data processing, we analyze the $q = 0$ superfluid fraction and subtract it from 1 to be γ_{MI} . We integrate the quasi-momentum distribution $n(q_x, q_y)$ (Fig. 6a) along y to obtain $n(q_x)$, as in the inset of Fig. 1c. To illustrate how we process the data, we plot Fig. 6b to help us explain each step. We exclude the background value, i.e. shift $n(|q_x| > \pi)$ to be zero. In the measurement of the band mapping, the central peak for the superfluid has a finite width due to the limit time of the time-of-flight. Because our method can give an exact-flat plateau in the deep MI region, we define the plateau to be of height $n(q_x \sim \pm\pi)$, and all deviations on top of this rectangle are regarded as the contributions of the superfluid. To avoid possible in-alignment errors, we re-define quasi-momentum zero to be the center of mass of the $n(q_x)$, and the symmetrization has been performed as $n_{q_x} \rightarrow (n_{q_x} + n_{-q_x})/2$. We obtain the

area of superfluid A_{SF} and total area $A_{tot.}$, the MI fraction is determined as:

$$\gamma_{MI} = 1 - \frac{A_{SF}}{A_{tot.}}. \quad (4)$$

Here γ_{MI} describes the fraction of decoherence. An increase of γ_{MI} means the disappearance of phase coherence or superfluid in our system.

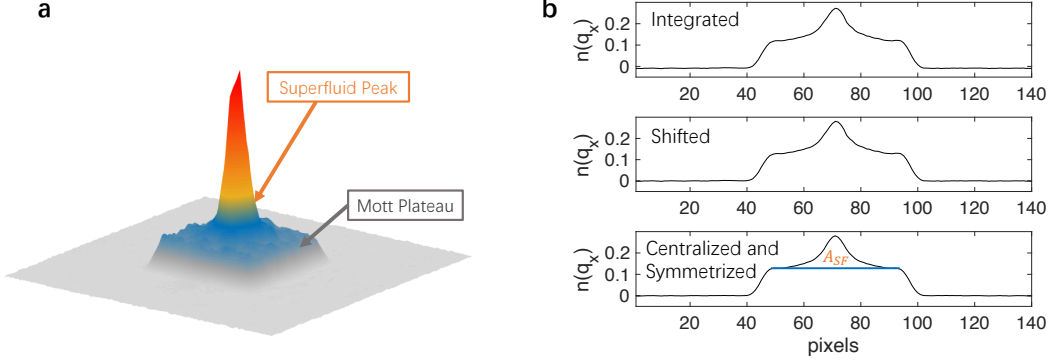


FIG. 6. **How to calculate γ_{MI} .** **a**, A band mapping profile consisting of two components of comparable fractions, the SF peak and the MI plateau. **b**, Integration of one dimension, background removal, and centralization with symmetrization. A_{SF} is defined in the lowest panel.

Measurement data error bars in Fig. 2 and 4

For each data point in Fig. 2 and 4 in the main text, we repeat the same measurements for 18 times, and group the samples as 3×6 . We average each 3 band mapping profiles and calculate γ_{MI} . The expected value and standard deviation of one specific data point are evaluated for such 6 groups. Based on our band-mapping method, the one standard deviation error bar is usually under 1% and smaller than the marker size.

Fitting lines in Fig. 2 and 4 and how to extract τ_{SF} , τ_{MI} , n_{ex} and A

In Fig. 2 and Fig. 4, the dynamics of various k under $4E_r/ms$ are fitted with polynomial with 6th order, while for $k > 4E_r/ms$ discrete data points are connected by spline interpolation. For τ_{MI} in Fig. 2, we cut at $\gamma_{MI} \in [0.85, 0.95]$ then average the delay time τ_{MI} obtained. While one could also fit every independent cut among the interval, then average the exponents obtained. We have examined that these two method result in nearly equal exponents. And for n_{ex} in Fig. 3, the vertical cut are set to be $V/E_r \in [18, 20]$ then we perform the same data processing stated above. The amplitude $A(k)$ in Fig. 4 is calculated by fitting $\gamma_{MI}(t)$ versus t in first $1.2ms$ to be $\gamma_{MI}(t) = A \cos(Bt + C) + D$, with error bar denoting fitting error.

Robustness of determination for power exponents

In the main text we show that by performing power law fitting to τ_{MI} versus k and n_{ex} versus k , different exponents are obtained. In principle, one could set an arbitrary cut bound to perform the fitting. Here we show that, among reasonable intervals, the cut bound does not influence the exponents obtained. In Fig. 7a, we set different potential depth, and the dependence of excitation fraction n_{ex} on k provides robust demonstration of $\nu z = 0.5 \pm 0.1$. And in Fig. 7b, in a range of $\gamma_{MI} \in [0.7, 0.9]$, the decay time shows a central value around $\nu z = 0.96 \pm 0.10$. Note that the νz indicated here are averaged values of data points in Fig. 7, and are different from those in main text, which are calculated by cutting specific bounds.

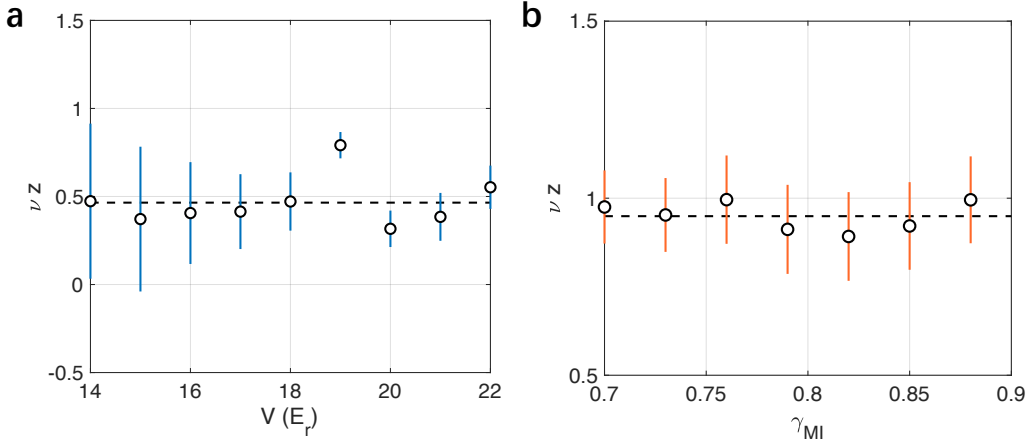


FIG. 7. **Robustness of the power fit.** **a**, The quantum critical parameter νz versus the cutting values of the trap depth V . νz is obtained from the excitation fraction $n_{ex}(k)$. **b**, νz versus the cutting values of γ_{MI} . νz is obtained from the Mott insulators delay time $\tau_{MI}(k)$: The dashed lines show averaged value of data points on graphs. Error bars correspond to one standard deviation.

Theoretical simulation

We simulate the experiment with Gutzwiller Mean Field Theory (GMFT)[? ?]. The many-body wave function is written as a product state:

$$|\Psi\rangle = \prod_i \sum_n f_i^n |n\rangle. \quad (5)$$

The mean field Hamiltonian can be decoupled as products of single sites Hamiltonians:

$$\begin{aligned} \hat{H}_{MF} &= \sum_{i,j} [-J(\psi_j a_i^\dagger + \psi_j^* a_i) + J\psi_i^* \psi_j] \\ &+ \frac{U}{2} \sum_i \hat{n}_i(\hat{n}_i - 1) + \sum_i \left(\frac{1}{2}m\omega_0^2 r_i^2 - \mu\right) \hat{n}_i \\ &= \sum_i h_{mf}, \end{aligned} \quad (6)$$

where $\psi_j = \langle \hat{a}_j \rangle$ refers to the local order parameter, m denotes the particle mass and ω_0 represents the vibrational frequency of the external harmonic trap. The simulation is performed in a 3D square lattice of 75^3 sites and all parameters are set to be exactly the same as those in our experiment. The chemical potential μ is set by the total particle number $N \sim 1.1 \times 10^5$. The local Hilbert space on every sites has cut-off $n_{max} = 7$ and the truncation errors are negligible. By solving minimization problem with respect to either $\langle \Psi | \hat{H} | \Psi \rangle$ or $\langle \Psi | \hat{H} - i \frac{\partial}{\partial t} | \Psi \rangle$, one could obtain the ground state under specific parameters or evolve the wavefunctions according to a time-dependent Hamiltonian respectively.

To resemble the MI fraction n_{ex} measured in the quasi-momentum profile, we define γ_{MI} as the fraction except zero-momentum condensation:

$$\gamma_{MI} = 1 - \sum_{i,j} \frac{\langle a_i^\dagger \rangle \langle a_j \rangle}{N}, \quad (7)$$

where N denotes total particle number.

A comparison to the experiment is shown in Fig. 8, where the dynamics of different γ_{MI} versus V are obtained. We see the both phenomena of a retarded relaxation and the phase oscillations in our GMFT calculations. However, the break down of the final thermalization in the deep MI region is due to that the mean field theory fails to capture the strongly interacting systems. To calculate τ_{SF} , we perform horizontal cut at $\gamma(t) = 0.6$ and find the coordinates of

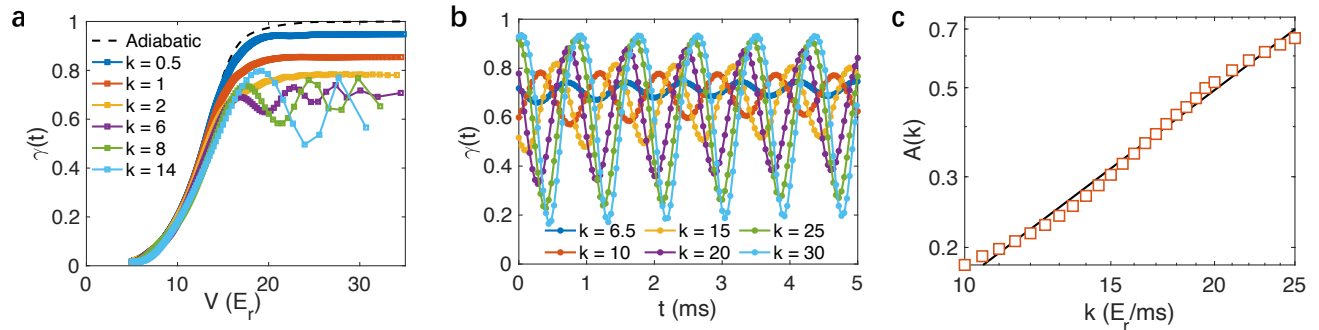


FIG. 8. **GMFT results.** **a**, γ_{MI} versus V depending on different ramping rate k . For $k \leq 4E_r/ms$, we see a retarded relaxation and γ_{MI} starts to oscillate when $k > 6E_r/ms$. **b**, The oscillations of γ_{MI} versus the holding time t . Following the same procedure in Fig. 4, we hold the sample at $V = 25E_r$ for a time t . Different ramping rates k result different oscillations of γ_{MI} . Based on this, we obtain the theoretical results in Fig. 4c in the main text. **c**, The oscillation amplitude at fast k plot versus k . The linear fitting is performed in log-log space and an exponent of 1.56(6) is obtained.

intersections $(V(k), 0.6)$ for each k , which is the same as in the data processing in our experiment. Excitation fractions n_{ex} are extracted from $V = 18E_r$, same as the experimental data. For a fast ramp $k > 12E_r/ms$, the amplitudes of the oscillations are calculated as the peak-to-peak values in Fig. 8b.